

# Tactile-based Exploration, Mapping and Navigation with Collision-Resilient Aerial Vehicles

Karishma Patnaik, Aravind Adhith Pandian Saravanakumaran and Wenlong Zhang\*

**Abstract**—This article introduces XPLORER, a passive deformable quadrotor UAV with a spring-augmented chassis and proprioceptive state awareness, designed to endure collisions and maintain smooth contact with the environment. A fast-converging external force estimation algorithm for XPLORER is designed to leverage onboard sensors and proprioceptive data for contact detection. Using this force information, four motion primitives are proposed, including three novel tactile-based primitives—tactile-traversal, tactile-turning, and ricocheting—to aid XPLORER in navigating unknown environments. These primitives are synthesized autonomously in real time to enable efficient exploration and navigation by leveraging collisions and contacts. Experimental results demonstrate the effectiveness of our approach, highlighting the potential of *passive* deformable UAVs for contact-rich real-world tasks such as non-destructive inspection, surveillance and mapping, and pursuit/evasion.

## I. INTRODUCTION

Conventional unmanned aerial vehicles (UAVs) often rely on external attachments for aerial-physical interaction tasks like grasping, perching, and pushing/pulling [1]–[6]. However, *reconfigurable* UAV designs can achieve similar functionalities with higher flight efficiency and safer interactions [7]–[9]. Most reconfigurable UAVs use *active* actuation mechanisms to alter their morphology, requiring meticulous planning and prior knowledge of the flight space [10]. In contrast, *passive* deformable UAVs are able to undergo a change in shape in response to external forces, intelligently harnessing collision energy for obtaining deformation by utilizing springs, origami structures, or soft bodies [11]–[15].

This article highlights the advantages of *passive* deformable UAVs for previously unexplored tasks such as tactile-based exploration and mapping, and agile navigation. Towards this, it introduces novel contact-based primitives and algorithms, expanding the applications of *passive* to many real-world tasks such as deformable UAVs to non-destructive inspection, surveillance and mapping, and pursuit/evasion.

## A. Related Literature

1) *External Wrench Estimation*: Augmenting a UAV with force-torque sensors is the most common approach to detect external wrench, but it increases the total weight of the UAV and adversely affects flight time [16], [17]. Alternatively, researchers have developed algorithms based on momentum-based [18], [19] and acceleration-based [20], [21] wrench

This material is based upon work supported by the National Science Foundation under Grant No. 2331781.

The authors are with School of Manufacturing Systems and Networks, Ira A. Fulton Schools of Engineering, Arizona State University, Mesa, AZ, 85212, USA. Email: {kpatnaik, apandial, wenlong.zhang}@asu.edu.

\*Address all correspondence to this author.

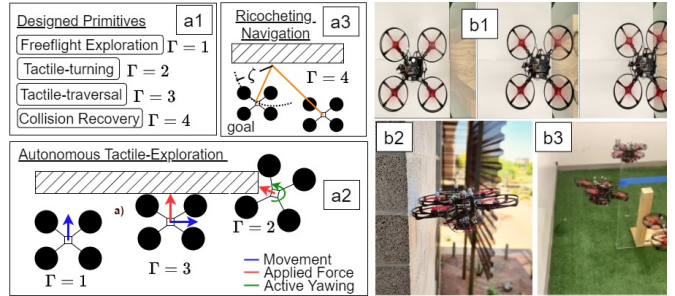


Fig. 1. An overview of the proposed tactile-based flight modes. (a1) The four primitives proposed in the article to facilitate autonomous exploration, mapping, and agile navigation with *passive* deformable UAVs. (a2)-(a3) Automatic online synthesis of  $\Gamma$  for tactile-based exploration and navigation. (b1) Sequence of slow-motion snapshots highlighting the chassis deformation upon contact. (b2) XPLORER enables tactile-based mapping of buildings using (a2). (b3) Ricocheting experiments for agile maneuvering using (a3).

estimators which rely on the available onboard sensors only such as inertial measurement units (IMUs). Kalman filtering approaches and hybrid methods, fusing momentum and acceleration-based wrenches, were proposed in [22], [23] for conventional UAVs. For this work, we aim to exploit *proprioceptive* information about the vehicle's morphology to improve the force estimate and identify the colliding arms.

2) *Static Force Application and Tactile-based Inspection*: Using the external wrench estimate, UAVs are now capable of performing tactile-based tasks such as non-destructive testing, vibration analysis and leak identification which require a desired wrench to be applied onto a surface in an attempt to reduce safety risks to human workers [24]–[28]. In this context, this work employs *passive* deformable quadrotors to establish smooth contacts and simplify the contact laws [29].

3) *Tactile-based Navigation*: Collision-resilient designs hold a strong potential for a paradigm shift for performing tactile-based navigation [30]–[34]. A motion planner for tactile-based navigation was proposed in [35] consisting of two modes, sliding and flying cartwheel. Authors of [36] utilized vision systems to navigate manhole-sized tubes along with flaps to sense contacts. In [37], collisions were exploited for path planning using sampling-based methods. However, all the works assume complete knowledge of the map of the environment a-priori. Autonomous navigation in an unknown environment is still nascent and remains an open problem.

4) *Mapping*: Conventionally, mapping an environment is performed by using cameras and Structure from Motion (SfM) technique [38] by recreating a 3D structure from a series of images captured from different angles. Research carried out in [39] used the combination of cameras, LiDAR, IMU, and encoders to generate a highly precise map of the environment. Another map generation methodology was

TABLE I

Symbol	Definition
${}_w\mathcal{F} = \{e_1, e_2, e_3\}$	inertial frame
${}_b\mathcal{F} = \{b_1, b_2, b_3\}$	body fixed frame
${}_a\mathcal{F} = \{a_1^i, a_2^i\}$	$i^{th}$ arm frame with $a_j^i \forall j = 1, 2$ denoting the basis vectors for the $i^{th}$ frame
$\mathbf{x} = [x \ y \ z]^T \in \mathbb{R}^3$	3D position of UAV in ${}_w\mathcal{F}$
$\dot{\mathbf{v}} = [\dot{x} \ \dot{y} \ \dot{z}]^T \in \mathbb{R}^3$	3D translational velocity of UAV in ${}_w\mathcal{F}$
$\mathbf{R} \in \mathbb{R}^{3 \times 3}$	rotation matrix from
$\psi \in \mathbb{R}, \dot{\psi} \in \mathbb{R}$	yaw and yawrate respectively
$\hat{\delta}_f \in \mathbb{R}^3$	net estimated force in ${}_w\mathcal{F}$
$\hat{\delta}_{\tau}^{e_3} \in \mathbb{R}$	estimated yaw torque in ${}_w\mathcal{F}$
$(\cdot)^{(\bullet)}$	specifies quantity $(\cdot)$ in $(\bullet)$ frame/direction
$\hat{\delta}^b \in \mathbb{R}^3 = [\hat{\delta}_f^{b_1} \ \hat{\delta}_f^{b_2} \ \hat{\delta}_f^{b_3}]^T$	denotes $\hat{\delta}_f$ in ${}_b\mathcal{F}$
$\mathbf{C}_n \in \mathbb{R}^4$	contact normal to the obstacle
$\lambda \in \{+X, +Y, -X, -Y\}$	current move direction of the vehicle
$d_{step} \in \mathbb{R}$	distance to move for each step
$\psi_0 \in \mathbb{R}$	yaw rate threshold
$\mathcal{W} \in \mathbb{R}$	Desired yaw rate
$\delta_0 \in \mathbb{R}$	force threshold to trigger <i>Tactile-traversal</i>
$\delta_{\psi_0} \in \mathbb{R}$	force threshold to trigger <i>Tactile-turning</i>
$\delta_{f_{des}} \in \mathbb{R}$	desired force to be applied on the obstacle
$\delta_{map} \in \mathbb{R}$	force threshold for mapping
$\Upsilon \in \mathbb{R}$	indicates if a contact is made by using $\theta_i$

presented in [23] where collision detection and localization were used to insert obstacle blocks into the point cloud map. However, autonomous planning for performing these missions in unknown low-visible environments where collisions are inevitable remains a challenge. Moreover, previously studied collision-based mapping [40], [41] are error-prone particularly when mapping curved surfaces, making continuous contact-based mapping a desirable approach, as shown in this paper.

### B. Contributions of Present Work

The main contributions of the article are:

- 1) Development of a fast-converging external force estimation algorithm for *deformable quadrotors* by utilizing proprioceptive information about the vehicle's morphology in addition to onboard accelerometer data.
- 2) Design of new tactile primitives—*tactile-traversal*, *tactile-turning*—for passive deformable UAVs to perform autonomous exploration of unknown environments and generate tactile-based maps.
- 3) Introduction of a novel 2D *Ricocheting* primitive for efficient braking in agile navigation to get minimum-time maneuvers by leveraging collision energy dissipation.

Figure 1 and Supplementary Video (Part1) showcase our compliant and passive deformable quadrotor, XPLORER, engaged in various contact-rich tasks. The rest of the article is structured as follows. Section II provides an overview of the design and low-level control of XPLORER. In Section III-A, we introduce the external force estimation algorithm, Section III-B introduces the reaction modes upon contact. Section IV presents the tactile-based missions and Section V presents the experimental results. Finally, Section VI concludes the article.

## II. DESIGN AND LOW-LEVEL CONTROL OF XPLORER

In this work, we use a modified version of the passive foldable aerial robot from our previous work [12]. Built on a

similar idea, XPLORER (shown in Fig. 1) has four deformable arms as part of its morphing chassis, but all four motors lie in a single plane. This design choice was made for two main reasons. The first was to lower the height of the center of mass (CoM) from our previous design (where the arms were in different planes) and prevent toppling when making contact with the environment. By having a CoM at a lower height, the toppling torque during contact is decreased due to the decrease in the lever arm length. Secondly, we ensure that the UAV will not be stuck in corner cases during exploration by redesigning the propeller guards, so a maximum of 30° of free rotation was feasible. Finally, the springs chosen for the current version are stiffer, restricting the collision-induced deformation to a maximum of 30°. This allows forces around 1N to be exerted on the environment without pitching significantly into the wall unlike the rigid ones (at least 5° pitch for a 1.3kg UAV with a thrust to weight ratio of 2.82).

The complete control block diagram is shown in Fig. 2 with the notations defined in Table I. Considering the net body thrust,  $f \in \mathbb{R}$ , and the body torques,  $\tau \in \mathbb{R}^3$ , as the control inputs, the rigid-body dynamics can be written as:

$$\dot{\mathbf{x}} = \mathbf{v} \quad (1a)$$

$$m\dot{\mathbf{v}} = mge_3 - f\mathbf{R}e_3 + \delta_f \quad (1a)$$

$$\dot{\mathbf{R}} = \mathbf{R}\hat{\Omega}$$

$$\mathbf{H}\dot{\Omega} - [\mathbf{H}\Omega]_{\times}\Omega = \tau + \delta_{\tau} \quad (1b)$$

where  $m$ ,  $\mathbf{H}$  denote the mass and inertia of XPLORER respectively, and  $\mathbf{x} \in \mathbb{R}^3$  and  $\mathbf{v} \in \mathbb{R}^3$  denote the 3D position and translational velocity, respectively. The other symbols and definitions adhere to literature [12]. The terms  $\delta_f \in \mathbb{R}^3$  and  $\delta_{\tau} \in \mathbb{R}^3$  denote the lumped external forces and torques respectively applied on the system. The *hat map*  $\hat{\cdot} : \mathbb{R}^3 \rightarrow \text{SO}(3)$  is a symmetric matrix operator such that  $\hat{\mathbf{x}}\mathbf{y} = \mathbf{x} \times \mathbf{y} \forall \mathbf{x}, \mathbf{y} \in \mathbb{R}^3$  and  $[\cdot]_{\times}$  is the skew symmetric cross product matrix.

The low-level tracking controller is a cascaded P-PID controller on the position and attitude errors as shown in Fig. 2. We leverage the inherent robustness of the P-PID control structure to maintain accurate tracking despite short-time ( $\approx 10^{\circ}$ ) arm angle deviations during collisions, which introduce minor inertia uncertainties.

## III. EXTERNAL FORCE ESTIMATION AND REACTION

In this section, we present a novel force estimator by fusing together the estimates based on the proprioceptive state of the vehicle and the accelerometer for faster convergence and collision arm isolation.

### A. Proposed External Force Estimation Algorithm

1) *Force estimate by the spring action at arm*: There are four reference frames  ${}_a\mathcal{F}, i = 1..4$ , for each arm as shown in Fig. 3. Now, considering the  $i^{th}$  arm and frame, torque estimate  $\delta_{\tau_i}^{a_i} \in \mathbb{R}$  can be computed by directly using the angular acceleration and rearranging the arm dynamics equation:

$$\mathcal{J}_{zz}\ddot{\theta}_i + b\dot{\theta}_i + k\theta_i = \delta_{\tau_i}^{a_i}, \quad \delta_{\tau_i}^{a_i} = \delta_{f_i}^{a_i}l \quad (2)$$

Here  $\mathcal{J}_{zz}$  is the inertia of the arm about the rotation axis,  $b$  and  $k$  are the damper and spring coefficients respectively and  $\theta_i$  is

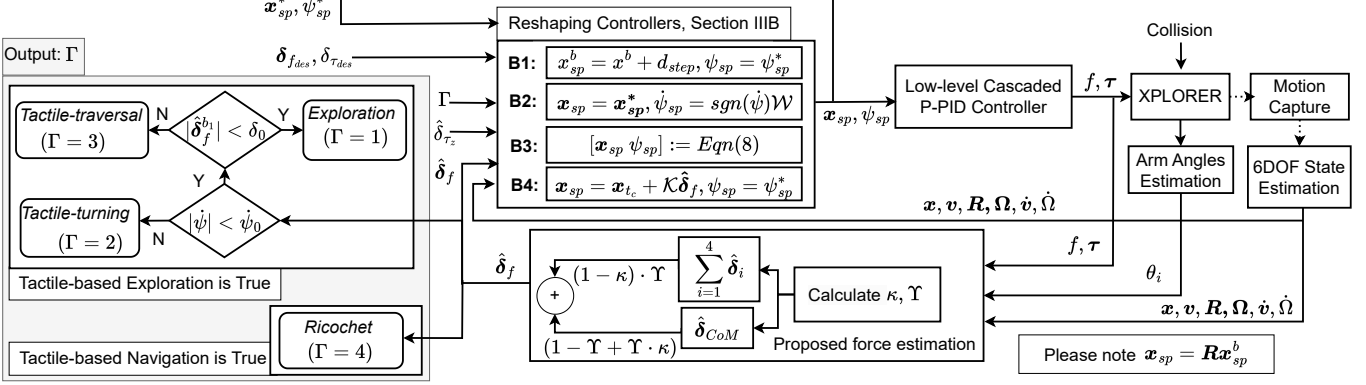


Fig. 2. Complete block diagram for autonomous exploration and navigation with XPLORE. The external contacts and collisions are characterized in the proposed force estimation block. This value is used to decide the state of exploration ( $\Gamma$ ) as shown by the state machine for exploration and navigation. For reference reshaping for each value of  $\Gamma$  is also shown which takes the inputs of the current reference,  $[x_{sp}^* \psi_{sp}^*]^T$ , desired interaction wrench  $[\delta_{f_{des}} \delta_{\tau_{des}}]^T$ .

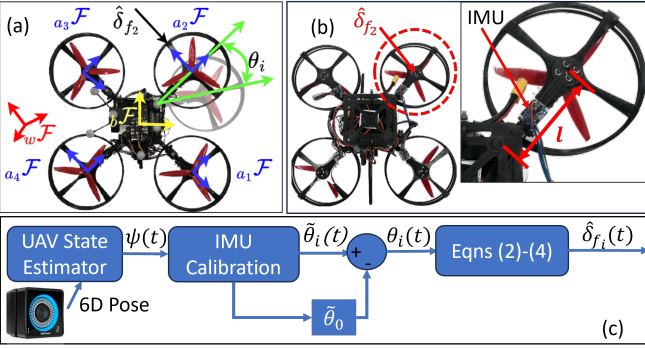


Fig. 3. (a) Frames used to estimate the external force on  $i^{th}$  arm,  $\hat{\delta}_{f_i}$  (b) A zoomed-in view to show the placement of IMU and the assumed point of application of  $\hat{\delta}_{f_i}$  (c) Block diagram for force estimation by spring action. the deflection in the angle for the  $i^{th}$  arm. The corresponding external force can be computed from  $\delta_{\tau_i}^{a_i} = \delta_{f_i}^{a_i} l$  by assuming that the point of application is at the motor center (which is approximately the arm CoM using SolidWorks estimate), at a constant distance  $l$  from the spring mounting location as shown by Fig. 3. Finally, a first order low-pass filter to estimate the external force in the arm frame,  $\hat{\delta}_{f_i}^{a_i} \in \mathbb{R}^2$ , since the angular acceleration can be noisy

$$\dot{\hat{\delta}}_{f_i}^{a_i} = [K_I(\delta_{f_i}^{a_i} - \hat{\delta}_{f_i}^{a_i}) \ 0]^T \quad (3)$$

where each element corresponds to the components in the direction of the  $i^{th}$  arm's two orthogonal basis and  $K_I$  denotes the filter gain. Now the external force on the  $i^{th}$  arm in the inertial frame denoted by  $\hat{\delta}_{f_i} \in \mathbb{R}^3$ , can be computed by the appropriate rotations (see Suppl. A)

$$\hat{\delta}_{f_i} = [{}^w R (\hat{\delta}_{f_i}^{a_i}) \ 0]^T \quad (4)$$

with  ${}^w R$  being the rotation from  $a_i \mathcal{F}$  frame to  $w \mathcal{F}$  frame.

2) *Force estimate from accelerometer at CoM*: Next, following [23], the force information can also be directly estimated from the acceleration measurement of the vehicle from the inertial measurement unit (IMU) of flight controller. Then, rearranging (1a) and using a median low-pass filter:

$$\hat{\delta}_{f_{CoM}} = m\dot{v} - mge_3 + fRe_3 \quad (5)$$

3) *Net estimated force on XPLORE*: The external force obtained from the IMU at CoM has a slower convergence rate than the arm-based estimate. Furthermore, if there is no

arm deflection from the external force (e.g. when the force is directly applied at CoM), the estimate based on only arm angle feedback does not converge to the true force, while the estimate from the CoM is correct in this case. In order to make the best use of the two resources and obtain a reliable force estimate, we combine the estimates from both methods. First, define an indicator function to detect contact on the arms

$$\Upsilon = \begin{cases} 1, & \text{if } \sum_{i=1}^4 |\theta_i| > \theta_{th} \\ 0, & \text{otherwise} \end{cases} \quad (6)$$

where  $\theta_i$  is the deflection angle of each arm, and  $\theta_{th}$  is the deflection threshold to detect contact, accounting for backlash. Next, our method for  $\hat{\delta}_f$  fuses (4) and (5) to give a fast and accurate estimate:

$$\hat{\delta}_f = (1 - \Upsilon + \Upsilon \cdot \kappa) \cdot \hat{\delta}_{f_{CoM}} + (1 - \kappa) \cdot \Upsilon \cdot \sum_{i=1}^4 \hat{\delta}_{f_i} \quad (7)$$

Here  $\kappa \in \mathbb{R}^3 = \xi \dot{\hat{\delta}}_{f_{CoM}} \triangleq h(\dot{\hat{\delta}}_{f_{CoM}})$  is an adaptive gain with the tuning parameter  $\xi$ .  $(\bullet)^{|\cdot|}$  denotes the element-wise absolute value of the vector  $(\bullet)$ . Based on (6) and (7), one gives higher weightage to  $\hat{\delta}_{f_{CoM}}$  during collision since the rate of change for  $\hat{\delta}_{f_{CoM}}$  is higher at the collision instant, so  $\kappa$  is larger and the CoM-based estimate is followed. On the other hand, when the wrench estimate from the CoM converges slowly, the rate of change is near zero making the term  $(1 - \kappa)$  is larger, so the total wrench converges to the arm-based estimate. The boundedness and convergence properties of the estimator in (7), and characteristics of  $h$  are discussed in Suppl. B. System identification for (2) is in Suppl. C. Finally, a momentum-based torque observer [23] is implemented to estimate the external torque  $\hat{\delta}_{\tau} \in \mathbb{R}^3$ . However, only the estimated yaw torque,  $\hat{\delta}_{\tau}^e \in \mathbb{R}$ , is utilized in tactile-based exploration of the following sections.

### B. Reaction Modes and Controllers for Reference Reshaping

We now introduce the various reference-generation controllers, which reshape the position, yaw, or both based on external wrench information, enabling different reaction modes.

For all the subsections that follow,  $x_{sp}^* \in \mathbb{R}^3$  and  $\psi_{sp}^* \in \mathbb{R}$  are the previous reference values of position and yaw respectively in  $w \mathcal{F}$  which are reshaped into  $x_{sp} \in \mathbb{R}^3$  and  $\psi_{sp} \in \mathbb{R}$  as the final the reference position and yaw, in  $w \mathcal{F}$ , for the low-level

controller to follow. The complete control block diagram with the interaction controller for XPLORER is shown in Fig. 2.

*Remark 1:* Note that whenever the references for exploration are generated in the body frame, we convert them into the inertial frame using the rotation matrix.

1) *Free-flight with position disturbance rejection:* In this state, at each instant the position reference in body frame for any one direction in  $x - y - z$  is generated using the current value. For example, if we need to only fly forward in  $b\mathcal{F}$ , only  $x^b$  will be reshaped, i.e.  $x_{sp}^b = x^b + d_{step}$  without  $y - z$  or yaw setpoint update. This mode is employed for free-flight exploration and tactile-traversal in Section IV-A.

2) *Continuous yawing:* The UAV *remains* at its current position ( $\mathbf{x}_{sp} = \mathbf{x}$ ) and continuously turns at a pre-specified constant yaw rate, i.e.  $\dot{\psi}_{sp} = \text{sgn}(\dot{\psi})\mathcal{W}$  where  $\mathcal{W}$  is a user defined constant,  $\text{sgn}$  denotes the sign function.

3) *Static-wrench application:* The reference is reshaped to exert a specific wrench on an object and navigate around it as described in Section IV-A. A position admittance control strategy is employed towards this by modeling the desired response as a virtual second-order dynamics [12], [23]:

$$\begin{bmatrix} m_v \mathbf{I}_{3 \times 3} & \mathbf{0}_{3 \times 1} \\ \mathbf{0}_{1 \times 3} & \mathcal{I}_{v,z} \end{bmatrix} \begin{bmatrix} \ddot{\mathbf{x}}_{sp} \\ \ddot{\psi}_{sp} \end{bmatrix} + \mathbf{D} \begin{bmatrix} \dot{\mathbf{x}}_{sp} \\ \dot{\psi}_{sp} \end{bmatrix} + \mathbf{K} \begin{bmatrix} \mathbf{x}_{sp} - \mathbf{x}_{sp}^* \\ \psi_{sp} - \psi_{sp}^* \end{bmatrix} = \begin{bmatrix} \hat{\delta}_f - \delta_{f,des} \\ \hat{\delta}_{\tau}^{e3} - \delta_{\tau,des} \end{bmatrix} \quad (8)$$

where  $\mathbf{x}_{sp}^*$  and  $\psi_{sp}^*$  are reshaped into  $\mathbf{x}_{sp}$  and  $\psi_{sp}$  respectively by using the external wrench and yaw-torque information -  $\hat{\delta}_f$  and  $\hat{\delta}_{\tau}$ . The virtual parameters employed to reshape the trajectory are the virtual mass,  $m_v \in \mathbb{R}^+$ , inertia about  $z$ ,  $\mathcal{I}_{v,z} \in \mathbb{R}^+$ , and the virtual damping and spring gain matrices,  $\mathbf{D} > 0 \in \mathbb{R}^{4 \times 4}$  and  $\mathbf{K} > 0 \in \mathbb{R}^{4 \times 4}$ .

4) *Collision recovery:* The reference is generated by utilizing the current location and the collision force. Specifically,  $\mathbf{x}_{sp} = \mathbf{x}_{t_c} + \mathcal{K}\hat{\delta}_f$  with a user defined constant  $\mathcal{K}$  and  $t_c$  denotes the collision instant. The yaw setpoint is not modified. We employ this reaction mode to execute novel *Ricochetting* maneuvers as will be described in Section IV-B.

#### IV. TACTILE-BASED MOTION PRIMITIVES AND MISSIONS

In this section, we present four primitives ( $\Gamma \in \{1, 2, 3, 4\}$ ), for novel tactile-based exploratory and navigation missions by deformable UAVs. We state the trigger conditions under which a primitive is autonomously engaged and the corresponding controllers from Section III-B that become active.

##### A. Case 1: Tactile-based Exploration and Mapping

1) *Tactile-based Exploration:* The exploration strategy is inspired by the coverage planning algorithms using a combination of random walk and wall tracing [42]. We introduce this exploration scheme to aerial robots for the first time, demonstrating its effectiveness for deformable UAVs over rigid ones due to the compliance enabling firm contacts.

The tactile-exploration scheme involves flying forward until encountering an object, then maintaining contact to slide along its surface and turning around its edges to follow its contours. Towards this goal, we define two online decision variables: the contact-normal direction  $\mathbf{C}_n$  and movement direction  $\lambda$ .

- The contact direction,  $\mathbf{C}_n \in \mathbb{R}^4$ , is four-element vector specifying the contact-normal of an object in  $\{b_1, -b_1, b_2\}$

or  $-b_2\}$  directions, with  $\|\mathbf{C}_n\|_1 = 1$ . For instance, if  $|b\hat{\delta}_f^{b_1}| > \delta_0$  and  $b\hat{\delta}_f^{b_1} < 0$ ,  $\mathbf{C}_n = [0 \ 1 \ 0 \ 0]$ , indicating an obstacle along  $\{b_1\}$  and the contact-normal along  $\{-b_1\}$ .

- The variable,  $\lambda$ , selects the next movement direction from  $\{b_1, b_2, -b_1$  or  $-b_2\}$  by cycling through the *ordered set*  $\{+X, +Y, -X, -Y\}$ . Formally,  $\lambda(k+4) = \lambda(k), \forall k \in \mathbb{Z}^+$  and  $k$  is the sample index.

We now present the novel tactile-primitives for exploration (details are shown in Suppl. D, Algorithms 1-3).

**Exploration:** Initially,  $\Gamma = 1$ , corresponding to free-flight exploration (referred hereon as simply *Exploration*) during which XPLORER experiences negligible yaw torques and external forces. The controller from Section III-B1 is utilized to generate the reference. We set  $d_{step}$  to fly “forward” in the body frame, i.e for  $\lambda = +X$ . The trigger condition for entering  $\Gamma = 1$  at any time, is  $(|\dot{\psi}| < \dot{\psi}_0)$  and  $(|\hat{\delta}_f^{b_1}| \text{ or } (|\hat{\delta}_f^{b_2}|)) < \delta_0$ .

**Tactile-turning:** At any moment, we monitor the yaw rate,  $\dot{\psi}$ , to detect turning around a point. This can occur when the vehicle slides along an object’s edge under a desired force, then releases contact at a corner, causing a sudden spike in  $\dot{\psi}$ . Thus, if  $|\dot{\psi}| > \dot{\psi}_0$ , where  $\dot{\psi}_0$  is the threshold, we set  $\Gamma = 2$ . We activate the continuous yawing controller from Section III-B2, allowing the vehicle to rotate around a corner point while monitoring  $\hat{\delta}_f^{b_1}$  (the force in  $\{b_1\}$  direction). If  $\hat{\delta}_f^{b_1} > \delta_{\psi_0}$  at any time, indicating that further turning is not feasible, we transition to the next exploration state. The threshold  $\dot{\psi}_0$  is chosen adequately to avoid false triggers and  $\psi_{sp}$  is bounded to  $[-\pi \ \pi]$  to avoid yawing indefinitely.

**Tactile-traversal:** This state is triggered when at any instant,  $|\hat{\delta}_f^{b_1}| \text{ or } |\hat{\delta}_f^{b_2}| > \delta_0$ , setting  $\Gamma = 3$ . The *Tactile-traversal* primitive enables sliding across an object while applying force on it utilizing the controllers from Sections III-B1 and III-B3. The movement direction  $\lambda$  is chosen from the cyclic sequence  $\{+X, +Y, -X, -Y\}$ , by monitoring  $\mathbf{C}_n$  in a direction opposite to current  $\lambda$ . For instance, if  $\lambda(k) = +X$  with  $\mathbf{C}_n = [0 \ 1 \ 0 \ 0]$ , then  $\lambda(k+1) = +Y$  following a right side rule.

For the above example, the next waypoint is first generated utilizing the controller in Section III-B1 with  $d_{step}$  for motion in  $+Y$ . The interaction controller from Section III-B3 then reshapes it to ensure that the vehicle maintains contact with the obstacle by exerting a desired force on it while flying across it, as shown in Fig. 1(ii). Specifically,  $\delta_{f,des} = [\Delta_{f,des} \ 0 \ 0]^T$  and  $\delta_{\tau,des} = \hat{\delta}_{\tau}^{e3}$  to enable force exertion in  $+X$ , flying in  $+Y$  and yielding to any yaw torques.

*Remark 2:* The force threshold check  $\delta_{\psi_0}$ , is chosen slightly higher than  $\delta_0$  to ensure fail-safe behavior while transitioning from  $\Gamma = 2$  to  $\Gamma = 3$ , such that in cases when it loses slight contact, a higher  $\delta_{\psi_0}$  will ensure *Tactile-traversal* can still be engaged immediately after *Tactile-turning*.

2) *Tactile-based Mapping:* The ability to explore the environment while maintaining contact can be utilized to generate an obstacle map to aid motion planning by XPLORER or other autonomous robots. The algorithm utilizes the  $\hat{\delta}_f$ , the CAD model of XPLORER, and the global pose to generate the obstacle boundary map. We use the Open3D library [43] to process the point cloud generated.

Obstacle map generation initializes if the estimated force is

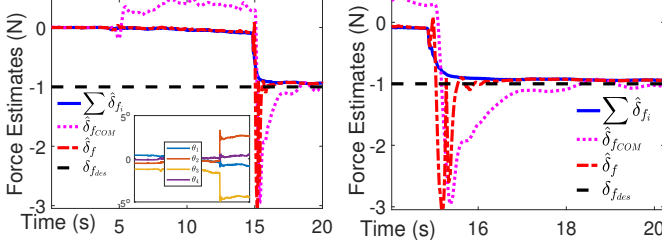


Fig. 4. Results for the proposed force estimation algorithm. Left: Shows estimates for  $\hat{\delta}_f$ ,  $\hat{\delta}_{f,COM}$  and  $\sum \hat{\delta}_f$ ; inset shows the corresponding deviation in arm angles. Right: zoomed-in view of the peak.

above the threshold, i.e.,  $|\hat{\delta}_f^{b_1}|$  or  $|\hat{\delta}_f^{b_2}| \geq \delta_{map}$ . As an additional condition, the mapping starts if the UAV is flying. A rigid object of dimension  $0.25 \text{ m} \times 0.08 \text{ m} \times 0.5 \text{ m}$  is added to the point cloud at a small offset from the CoM of XPLOTER in the direction of  $C_n$ , which provides the outward normal of the obstacle. This mimics the boundary being traced. To account for corner cases, we also monitor the previous and current move directions,  $\lambda(k-1)$  and  $\lambda(k)$  to decide the object placement. For corners, where the move direction  $\lambda(k)$  is not the same as the previous move direction  $\lambda(k-1)$ , a fixed point cloud is added diagonally with an offset of  $0.417 \text{ m}$  to the map to make it continuous around the corners. These parameters were selected to fit the indoor environment conditions and provide accurate maps of the objects.

The point cloud map is generated at a frequency of 30 Hz to achieve a high-resolution representation of the obstacle. It is stored in Polygon File Format (PLY) in ASCII format, containing the coordinates of each point in the cloud. The map generation process was carried out on a computer equipped with an AMD Ryzen 5 CPU and 16GB of RAM. The position and wrench estimates are recorded on the ground computer and relayed from the high-level companion computer via ROS2 network. An overview of the framework is in Suppl. Alg. 4.

### B. Case 2: Tactile-based Navigation - Ricocheting

We now present a new maneuver, *Ricocheting*, enabled by collision-resilient quadrotors to decelerate and achieve a sudden change in momentum by bouncing-off objects.

First, we collected experimental data for six different collision velocities with two different heading angles (at  $\psi = 90^\circ$ ,  $45^\circ$ ) with five trials each, totaling 60 flights to understand the post-collision dynamics. In all the experiments, the recovery controller from Section III-B4 is employed to generate the post collision waypoint. The scatter plots for these experiments are shown in Fig. 5, along with the error ellipses. We noticed that the heading angle didn't influence the post collision state significantly. Moreover, in all the experiments, there was energy loss due to the damping introduced by the deformable chassis resulting in dissipation of energy which combined with the recovery controller, facilitates a fast stopping maneuver.

This enables us to define *Ricocheting* ( $\Gamma = 4$ ), as a maneuver where collisions between the UAV and environment serve as jump maps to facilitate minimum-time trajectories. Following the time-optimal control approach for hybrid double integrators with state-driven jumps in [44], simulation results in Fig. 5(b) show that the path 1-2-3-4-5 is shorter than 1-4-5 when

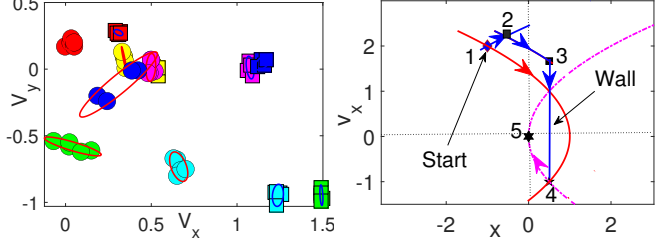


Fig. 5. Left: Collision experiments to understand ricocheting. Symbols  $\square$  and the  $\circ$  represent the pre and post-collision velocities of each case (distinguished by color). For significant range of velocities, the recovery controller and the deformable chassis of XPLOTER facilitate efficient braking maneuvers with collisions. Right: Simulation phase-portrait to demonstrate ricocheting (path 1-2-3-4-5) vs conventional (path 1-4-5). The curves represent constant acceleration for a second order system,  $\ddot{x} = u$ , with  $u$  as the input.

state jumps are allowed (the complete derivation is in Suppl. F). However, the UAV ricocheting problem differs from the setting in [44] because collisions serve as jump maps, which cannot be activated arbitrarily. Therefore, we developed a neural network (CollisionNet) to predict the rebound velocities for the data collected (details in Suppl. E) and introduce a modification to decide whether or not to ricochet:

*Ricocheting Condition:* If a collision node lies within a circle of  $\zeta$  radius of the stopping node (marked in Fig. 1(a3)), incorporate a collision off that node at maximum velocity attainable for a minimum-time maneuver to reach the stopping node. The pre-collision velocities can be verified via the CollisionNet developed. We choose  $\zeta = 0.5 \text{ m}$ .

*Remark 3:* In most experiments, collisions introduced an undesired downward force, so we avoid exploiting momentum changes along  $e_3$  and focus only on in-plane (2D) collisions (hence a circle in above condition). Moreover, as heading angle changes have a minor impact on momentum relative to the pre-collision velocity, any 2D maneuver can be effectively reduced to 1D for multirotor UAVs, ensuring the condition is valid.

*Remark 4:* There is significant variation in the post collision state at higher velocities (large blue and green scatter groups in Fig. 5) warranting thorough collision modeling for impact dynamics which is outside the scope of this paper.

## V. EXPERIMENTAL RESULTS AND DISCUSSION

### A. Experimental Setup, Sensors and Control Parameters

1) *Hardware, Software, and Physical Setup:* The low-level controller utilized is a PIXHAWK flight controller with the RaspberryPi4B as the companion computer. We utilize the companion computer to relay the position and orientation of the vehicle from an indoor motion capture system to the flight controller at 120 Hz. A 4S lithium polymer battery of 3300 mAh LiPo battery of 14.8V, 50C is used for the power supply. The motors are controlled utilizing Lumenier 30A BLHeli\_S Electronic Speed Controllers and the entire system has a mass of 1.12 kg. Our experimental testbed consists of four distinct environments which closely resemble real-world flight spaces and help in validating the tactile-based exploration and navigation algorithms. (i) a rectangular object measuring  $1.22 \text{ m} \times 1.0 \text{ m}$  was set up using acrylic panels (ii) acrylic panels were organized to represent a box with XPLOTER's initial

TABLE II  
PARAMETERS & THRESHOLDS USED IN EXPERIMENTS

Parameter	Threshold Value	Parameter	Threshold Value
$\dot{\psi}_0$	0.4 rad/s	$d_{step}$	0.25 m
$\mathcal{W}$	0.26 rad/s	$\Delta_{f_{des}}$	1.25 N
$\delta_0$	1.5 N	$\delta_{map}$	1.51 N
$\delta_{\psi_0}$	1.6 N	$\mathcal{K}$	0.1

state outside the box (iii) a trash can and (iv) a vertical pipe to represent real obstacles.

2) *Sensors, Measurements for Arm- and CoM-based force/torque estimates*: We employ four low-cost off-the-shelf 9-DOF IMUs (BNO055, Adafruit, New York, NY) on XPLORE (one on each arm) to get the angular acceleration and estimate the external force on the arm. They are connected to the companion computer via serial communication at 50 Hz. The Euler angles are computed using the Adafruit BNO055 library. A median low-pass with a band-stop filter is employed to obtain accurate estimates of the arm angles,  $\theta_i$ , at any given instant. This is used to estimate the arm wrench  $\hat{\delta}_{f_i}$  in (4).

3) *Thrust Estimate and Parameters of Interaction Controller*: In order to calculate the wrench at the CoM, the controller's normalized force and torque values are obtained from the onboard flight controller. The force value is obtained empirically and used to calculate the approximate value of the actual thrust. This technique can be improved by performing a PWM-thrust mapping curve using RPM sensor feedback. Gains for the interaction controller in (8) are tuned by experiments to be:  $\mathbf{D} = \mathbf{K} = diag(24.5, 24.5, 0, 1)$ ,  $m_v = \mathcal{I}_{v,z} = 1$ .

### B. Force Estimation Algorithm Validation

A static wrench application task is performed to validate the force estimation algorithm as shown in Fig. 4. The reference for this experiment is set to  $\delta_{f_{des}} = [-1 \ 0 \ 0]^T$  for applying a 1 N force on the wall. We use a load cell (ATO Micro 5kg Tension and Compression Load Cell, S Type, ATO, Diamond Bar, CA) with a sampling rate of 20Hz, mounted on the wall, to obtain the ground truth. A digital reader is attached to the load cell which is calibrated to display the force readings when the load cell is compressed. The UAV takes off and starts applying force on the box whose other end pushes the load cell. Wrench validation experiments are shown in Supplementary Video, SVideo (Part2).

The inset plot in Fig. 4, shows the deviation of the arm angles upon contact. The estimate from the CoM (magenta dotted line) takes time to converge, however, the arm-based force estimate (blue solid) converges sooner without the collision peak. By fusing both methods, the proposed estimate (red dashed) retains the peak from the CoM-based method and also converges faster. For this experiment, the true force applied on the wall was collected and averaged over 2s after impact, to be approximately 1.31 N, demonstrating an accuracy of  $\approx 77\%$ . We also conduct experiments where there is no contact to show  $\hat{\delta}_f = \hat{\delta}_{f_{CoM}}$  (SVideo Part2 pulley experiment).

### C. Autonomous Tactile-based Exploration and Mapping

In this section, we discuss the experimental results for the exploration and mapping mission of Section IV-A1 applied to map a wall-like structure, a box-like structure, an acrylic pipe and a trash can as shown in Figs. 6 and 7.

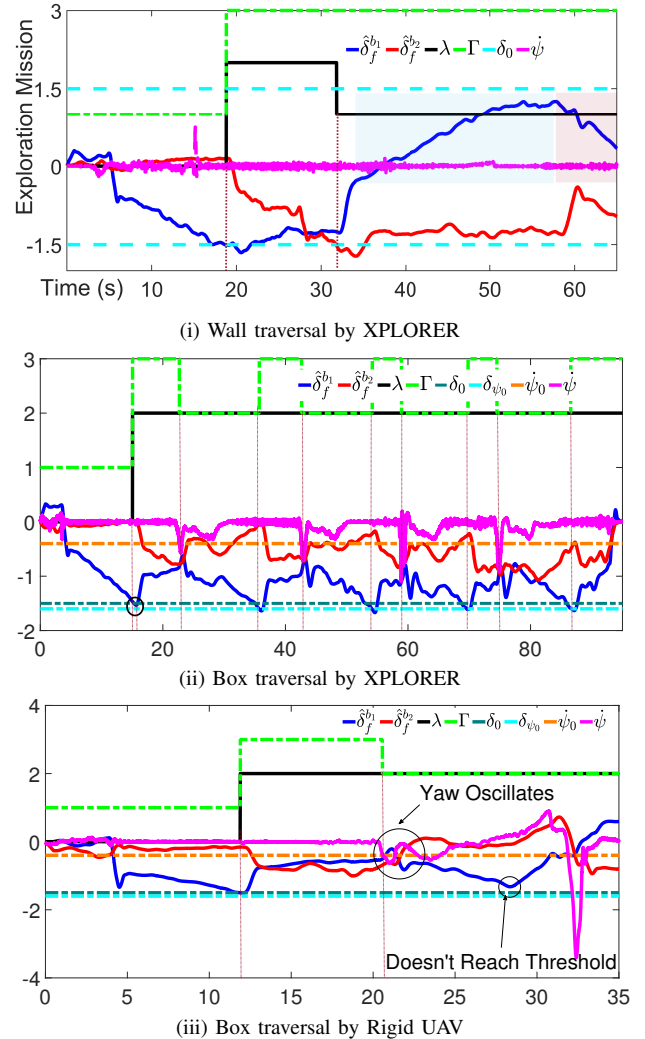


Fig. 6. Experimental results for tactile-based exploration. (i) Results of XPLORE for a wall-like structure. The exploration states are triggered when the threshold for  $\delta_0$  is crossed. In this case, only two states corresponding to  $\Gamma = 1$  and 3 are activated. The blue and red regions indicate the presence of unmodeled frictional and wall-effects. (ii) Results of XPLORE for a box-like structure. The exploration states are switched when the thresholds for  $\delta_0$  or  $\dot{\psi}_0$  are crossed. In this case, all three states corresponding to  $\Gamma = 1, 2, 3$  are activated. (iii) Results of rigid UAV for exploring convex corners. At the corners, the absence of compliance in the chassis brings about oscillatory yaw motion, failing to engage *Tactile-traversal* after *Tactile-turning*.

The mission starts with XPLORE taking off to a hover height of 0.7 m and initiating *Exploration* ( $\Gamma = 1$ ) to move forward. Upon detecting an obstacle, it pushes against it until the threshold for *Tactile-traversal* is reached. At that point, it switches to *Tactile-traversal* ( $\Gamma = 3$ ), sliding along the obstacle's surface. This transition from  $1 \rightarrow 3$  is shown in Fig. 6i. If the vehicle encounters an outward corner (such as on a box) causing a sudden yaw, it enters the *Tactile-turning* state ( $\Gamma = 2$ ) to perform a controlled yaw and establish contact with the adjacent surface, then returns to *Tactile-traversal* ( $\Gamma = 3$ ). For box-like structures, the sequence is  $1 \rightarrow 3 \rightarrow 2 \rightarrow 3$ , illustrated in Fig. 6ii. XPLORE continues sliding along each edge until it completes a full loop back to the initial contact point, then flies in another direction to continue exploring. The corresponding mapping results are shown in insets of Fig. 7.

The performance of exploratory algorithm relies on the thresholds specified which are in turn influenced by the

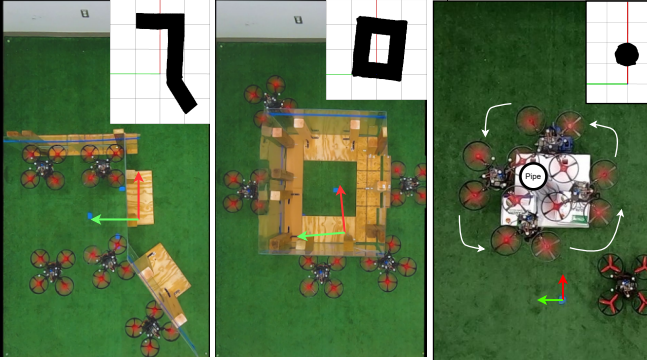


Fig. 7. Top view of the mapping experiments with the corresponding maps generated, in the insets for a box, a wall and an acrylic pipe.

unmodeled friction and aerodynamic wrenches. With extensive testing, we determined the threshold values for these parameters that work well in indoor environments as listed in Table II. Additionally, the state machine employs a moving average filter with 50 samples to filter  $\hat{\delta}_f$ , and a low-pass filter on the yaw rate  $\dot{\psi}$  to reduce noise effects on decision making.

1) *Wall-traversal*: In this experiment, XPLOREER navigates across a wall edge.  $\Gamma$  switches between 1 and 3 only as shown by the green line in Fig. 6i and SVideo (Part3a); the yaw-rate never crosses  $\dot{\psi}_0$  for *Tactile-turning* to be engaged. The mapping algorithm follows the description in Section IV-A2 and the generated map is shown in inset of Fig. 7.

2) *Box-traversal*: In this experiment, XPLOREER navigates around a box. From Fig. 6ii we can infer that  $\Gamma$  switches between values of 1, 2 and 3 whilst circumnavigating the obstacle. We measure the dimension of the box from the generated map (in the inset of Fig. 7) as  $1.231 \text{ m} \times 1.019 \text{ m}$  and the actual dimensions are  $1.22 \text{ m} \times 1.0 \text{ m}$ . The accuracy is about 96.72% for computing the area of the box. One source of mapping error can be the errors in the motion capture system used in our experiment, which aggregate and affect the point cloud data. The results are shown in SVideo (Part3b).

3) *Pipe outer diameter traversal*: This test case effectively demonstrates the tactile-based exploration algorithm's capability to navigate circular objects. The generated map in the inset of Fig. 7 and SVideo (Part3c) for this particular scenario, however is within 86% of the actual dimensions of the pipe, possibly due to instances when XPLOREER momentarily loses contact with the pipe before re-establishing contact.

4) *Trash can traversal*: This case presents a partial success scenario when during tactile-based exploration, XPLOREER loses contact (final edge of the trash can in SVideo (Part3c)). The low-friction surface and the dimension of the can relative to XPLOREER's width, likely result in insufficient  $\dot{\psi}$  at the corner, preventing the system from entering the *Tactile-turning* state. The mission is manually terminated here. In future, design modifications and online tuning of controller parameters can be looked into to prevent such failures.

5) *Comparison against a Rigid UAV*: We conducted both wall-traversal and box-traversal experiments for a similar dimension rigid UAV and only the wall-traversal exploration with inward edges was successful. For a box-like obstacle, the rigid UAV initially is successful in engaging  $\Gamma$  as  $1 \rightarrow 3 \rightarrow 2$

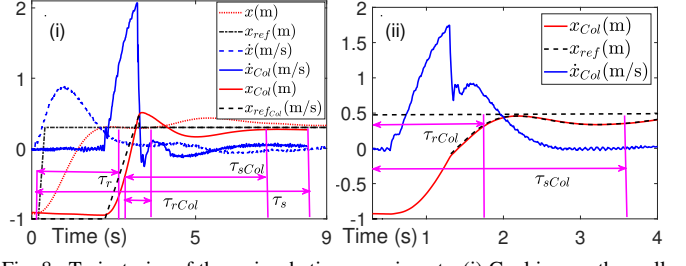


Fig. 8. Trajectories of three ricocheting experiments. (i) Goal is near the wall, shows both with- and without- ricocheting. (ii) Goal location is beyond wall, ricocheting off the edge. In all cases, ricocheting maneuvers are time-optimal.

systematically as shown by the green line in Fig. 6iii. However, after the turning maneuver in  $\Gamma = 2$ , significant oscillations are observed in yaw and the UAV was not able to maintain consistent contact, possibly due to absence of compliance and damping in the chassis. Consequently,  $\Gamma = 3$  was never engaged as compared to the XPLOREER case, where reengagement happened around 37s as shown in Fig. 6ii. Similar behaviors are observed in all four experiments conducted for this case, and the exploration scheme for a rigid drone failed. Experimental videos are presented in SVideo (Part3d).

*Note:* Additional validation results are presented in SVideo Part3c for objects with slots. It is also observed that in some cases when the rigid UAV makes a contact in *Exploration* state, significant yaw torque disturbance (due to the large impacts) falsely triggered the *Tactile-turning* state, reinforcing that the proposed tactile-based exploration scheme is suitable for deformable UAVs. These results are presented in Suppl. E.

#### D. Waypoint Tracking via Ricochetting

We now present two cases to demonstrate benefits of ricochetting. In the first case, the goal  $([0.3 \ 0 \ -0.75]^T \text{ m})$  is near the wall ( $x_{wall} = 0.5 \text{ m}$ ) to facilitate *ricocheting off the wall's face* with a velocity of  $[\dot{x}^-, \dot{y}^-]^T = [2, 0]^T \text{ m/s}$ . In the second case, the goal  $([0.5 \ 0 \ -0.75]^T \text{ m})$  is set some distance beyond the wall ( $x_{wall} = 0 \text{ m}$ ) to enable *ricocheting off the edge* with  $[\dot{x}^-, \dot{y}^-]^T = [1.75, 0]^T \text{ m/s}$ . For both the cases, the start location is  $[-1 \ 0 \ -0.75]^T \text{ m}$ . The pre-collision velocities were maximum velocities that could be attained in the closed space and are duly verified by the CollisionNet in Section. IV-B to have reduced rebound velocities upon impact.

The rise time ( $\tau_r$ ) and the settling time ( $\tau_s$ ) are chosen as the metrics to evaluate the performance of ricochetting. Comparison with the conventional, collision-exclusive trajectory is shown in Fig. 8i, where the vehicle first accelerates, then decelerates to reach the setpoint. There is an overshoot which it tries to minimize, slowly converging to the reference. The  $\tau_r$  and  $\tau_s$  are noted to be 2.27 and 8.995 seconds, respectively. Furthermore, over three trials the RMSE error was around  $\pm 3 \text{ cm}$  for this case. In contrast, the experimental results for ricochetting show that XPLOREER reaches the wall with maximum velocity, collides, and stops at the wall almost instantaneously by dissipating kinetic energies as shown by the plots in Fig. 8i. The  $\tau_{rCol}$  (subscript  $Col$  denotes experiments with collision) and  $\tau_{sCol}$  are calculated to be 1.046 and 5.292 seconds, respectively which are faster than the conventional trajectories. For the case where the vehicle performs rico-

cheting and regulates itself to a setpoint beyond the wall, and results in Fig. 8ii show significantly shorter convergence time with  $\tau_{rCol} = 1.685$  seconds and  $\tau_{sCol} = 3.631$  seconds, respectively. We also noted that the RMSE values over six trials for the collision-inclusive trajectories were  $\pm 0.5\text{cm}$  showing improved tracking accuracy than the conventional maneuvers. The flight test results are shown in SVideo (Part4).

## VI. CONCLUSION

In this work, we presented an *autonomous exploration and navigation* framework for passive deformable quadrotors, to explore unknown environments through contact. An external force estimation algorithm was proposed using proprioceptive information and the proposed exploration and mapping scheme was successfully verified in experiments. Finally, a novel ricochet maneuver was introduced which generated minimum-time paths by exploiting collision-induced state jumps. These novel flight modes enable future UAVs to perform autonomous contact-rich tasks such as inspection, manipulation, and aggressive maneuvers in cluttered environments.

Future work will look into utilizing visual inertial odometry for position estimates, performing adaptive adjustments of desired interaction parameters for a firm contact with any object and planning ricochet maneuvers in real-time. Furthermore, detailed contact modeling will be explored to develop new collision-aware recovery controllers and motion planners.

## VII. ACKNOWLEDGMENTS

The authors thank YiZhaung Garrard, Bill Nguyen and Yogesh Kumar from the ASU RISE lab for the brainstorming sessions and help with experiments.

## REFERENCES

- [1] F. Ruggiero *et al.*, “Aerial manipulation: A literature review,” *IEEE Robot. Autom. Lett.*, vol. 3, no. 3, pp. 1957–1964, 2018.
- [2] D. Hausamann *et al.*, “Monitoring of gas pipelines—a civil uav application,” *Aircraft Eng. Aero. Tech.*, vol. 77, no. 5, pp. 352–360, 2005.
- [3] S. Mishra *et al.*, “Autonomous vision-guided object collection from water surfaces with a customized multirotor,” *IEEE/ASME Trans. Mech.*, vol. 26, no. 4, pp. 1914–1922, 2021.
- [4] S. Kim *et al.*, “Aerial manipulation using a quadrotor with a 2dof robotic arm,” in *IEEE/RSJ Int. Conf. Int. Robot. Sys.*, pp. 4990–4995, 2013.
- [5] A. Suarez *et al.*, “Lightweight compliant arm for aerial manipulation,” in *IEEE/RSJ Int. Conf. Int. Robot. Sys.*, pp. 1627–1632, 2015.
- [6] A. Bredenbeck *et al.*, “Embodying compliant touch on drones for aerial tactile navigation,” *IEEE Robot. Autom. Lets.*, vol. 10, no. 2, pp. 1209–1216, 2024.
- [7] M. Kovac, “Learning from nature how to land aerial robots,” *Science*, vol. 352, no. 6288, pp. 895–896, 2016.
- [8] S. Mintchev and D. Floreano, “Adaptive morphology,” *IEEE Robot. Autom. Mag.*, vol. 23, no. 3, pp. 42–54, 2016.
- [9] W. Tao *et al.*, “Design, characterization and control of a whole-body grasping and perching (WHOPPER) drone,” in *IEEE/RSJ Int. Conf. Int. Robot. Sys.*, pp. 1–7, IEEE, 2023.
- [10] K. Patnaik and W. Zhang, “Adaptive attitude control for foldable quadrotors,” *IEEE Control Systems Letters*, 2023.
- [11] K. Patnaik and W. Zhang, “Towards reconfigurable and flexible multirotors,” *Int. J. Intel. Robot. App.*, vol. 5, no. 3, pp. 365–380, 2021.
- [12] K. Patnaik *et al.*, “Design and control of squeeze,” in *IEEE/RSJ Int. Conf. Int. Robot. Sys.*, pp. 1364–1370, 2020.
- [13] Z. Liu and K. Karydis, “Toward impact-resilient quadrotor design, collision characterization and recovery control to sustain flight after collisions,” in *IEEE Int. Conf. Robot. Autom.*, pp. 183–189, 2021.
- [14] K. Patnaik *et al.*, “Collision recovery control of a foldable quadrotor,” in *IEEE/ASME Int. Conf. Adv. Int. Mech.*, pp. 418–423, 2021.
- [15] P. H. Nguyen, K. Patnaik, *et al.*, “A soft-bodied aerial robot for collision resilience and contact-reactive perching,” *Soft Robotics*, 2023.
- [16] V. Serbezov *et al.*, “Application of multi-axis force/torque sensor system,” *IOP Conf. Mater. Sci. and Eng.*, vol. 878, no. 1, p. 012039, 2020.
- [17] A. Ollero *et al.*, “The aeroarms project,” *IEEE Robot. Autom. Mag.*, vol. 25, no. 4, pp. 12–23, 2018.
- [18] F. Ruggiero *et al.*, “Impedance control of vtol uavs with a momentum-based external generalized forces estimator,” in *IEEE Int. Conf. Robot. Autom.*, pp. 2093–2099, 2014.
- [19] F. Ruggiero *et al.*, “Passivity-based control of vtol uavs with a momentum-based estimator of external wrench and unmodeled dynamics,” *Robot. Auto. Sys.*, vol. 72, pp. 139–151, 2015.
- [20] B. Yüksel *et al.*, “A nonlinear force observer for quadrotors and application to physical interactive tasks,” in *IEEE/ASME Int. Conf. Adv. Int. Mech.*, pp. 433–440, 2014.
- [21] M. Ryll *et al.*, “6d interaction control with aerial robots: The flying end-effector paradigm,” *Int. J. Robot. Research*, vol. 38, no. 9, pp. 1045–1062, 2019.
- [22] C. D. McKinnon and A. P. Schoellig, “Unscented external force and torque estimation for quadrotors,” in *IEEE/RSJ Int. Conf. Int. Robot. Sys.*, pp. 5651–5657, 2016.
- [23] T. Tomic *et al.*, “External wrench estimation, collision detection, and reflex reaction for flying robots,” *IEEE Trans. Robot.*, vol. 33, no. 6, pp. 1467–1482, 2017.
- [24] P. Pfandler *et al.*, “Flying corrosion inspection robot for corrosion monitoring of civil structures—first results,” in *SMAR Conf. on Smart Moni. Assess. Rehab. Civil Struc. Prog.*, pp. We–4, 2019.
- [25] J. Hu, S. Zhang, E. Chen, and W. Li, “A review on corrosion detection and protection of existing reinforced concrete (rc) structures,” *Construction and Building Materials*, vol. 325, p. 126718, 2022.
- [26] K. Alexis *et al.*, “Aerial robotic contact-based inspection: planning and control,” *Autonomous Robots*, vol. 40, pp. 631–655, 2016.
- [27] K. Bodie *et al.*, “Active interaction force control for contact-based inspection with a fully actuated aerial vehicle,” *IEEE Trans. Robot.*, vol. 37, no. 3, pp. 709–722, 2020.
- [28] M. Tognon *et al.*, “A truly-redundant aerial manipulator system with application to push-and-slide inspection in industrial plants,” *IEEE Robot. Autom. Lett.*, vol. 4, no. 2, pp. 1846–1851, 2019.
- [29] B. Brogliato, *Nonsmooth mechanics*, vol. 3. Springer, 1999.
- [30] J.-C. Zufferey, A. Beyeler, and D. Floreano, “Optic flow to steer and avoid collisions in 3d,” *Flying Insects and Robots*, pp. 73–86, 2010.
- [31] D. Schafroth, S. Bouabdallah, C. Bremes, and R. Siegwart, “From the test benches to the first prototype of the mufly micro helicopter,” *J. Intel. Robot. Sys.*, vol. 54, pp. 245–260, 2009.
- [32] R. He, A. Bachrach, and N. Roy, “Efficient planning under uncertainty for a target-tracking micro-aerial vehicle,” in *IEEE Int. Conf. Robot. Autom.*, pp. 1–8, 2010.
- [33] S. Shen, N. Michael, and V. Kumar, “Autonomous multi-floor indoor navigation with a computationally constrained mav,” in *IEEE Int. Conf. Robot. Autom.*, pp. 20–25, 2011.
- [34] D. Scaramuzza *et al.*, “Vision-controlled micro flying robots,” *IEEE Robot. Autom. Mag.*, vol. 21, no. 3, pp. 26–40, 2014.
- [35] N. Khedekar *et al.*, “Contact-based navigation path planning for aerial robots,” in *Int. Conf. Robot. Autom.*, pp. 4161–4167, IEEE, 2019.
- [36] P. De Petris *et al.*, “Resilient collision-tolerant navigation in confined environments,” in *IEEE Int. Conf. Robot. Autom.*, pp. 2286–2292, 2021.
- [37] J. Zha and M. W. Mueller, “Exploiting collisions for sampling-based multicopter motion planning,” in *IEEE Int. Conf. Robot. Autom.*, pp. 7943–7949, 2021.
- [38] J. L. Schonberger and J.-M. Frahm, “Structure-from-motion revisited,” in *Proc. IEEE Conf. Comput. Vis. Patt. Recog.*, pp. 4104–4113, 2016.
- [39] D. Cattaneo *et al.*, “Cmrnet: Camera to lidar-map registration,” in *IEEE Intel. Transp. Sys. Conf.*, pp. 1283–1289, 2019.
- [40] Y. Mulgaonkar *et al.*, “The tiercel: A novel autonomous micro aerial vehicle that can map the environment by flying into obstacles,” in *Int. Conf. Robot. Automation*, pp. 7448–7454, IEEE, 2020.
- [41] A. Briad *et al.*, “Contact-based navigation for an autonomous flying robot,” in *IEEE/RSJ Int. Conf. Int. Robot. Sys.*, pp. 3987–3992, 2013.
- [42] K. M. Hasan *et al.*, “Path planning algorithm for autonomous vacuum cleaner robots,” in *Int. Conf. Info. Elec. Vis.*, pp. 1–6, IEEE, 2014.
- [43] Q.-Y. Zhou, J. Park, and V. Koltun, “Open3D: A modern library for 3D data processing,” *arXiv:1801.09847*, 2018.
- [44] A. Cristofaro *et al.*, “Time-optimal control for the hybrid double integrator with state-driven jumps,” in *IEEE Conf. Decision. Control.*, pp. 6301–6306, 2019.

## APPENDIX

### A. Rotation from the Arm Frame to Body Frame

The rotation matrix for converting a vector in the arm frame  ${}_a\mathcal{F}$ , to body frame  ${}_b\mathcal{F}$ , is given by (9) below

$${}_{a_i}^b\mathbf{R} = \begin{bmatrix} \cos \varphi_i & -\sin \varphi_i & 0 \\ \sin \varphi_i & \cos \varphi_i & 0 \\ 0 & 0 & 1 \end{bmatrix} \quad (9)$$

with  $\varphi_i$  being the arm angle deflection for the  $i^{th}$  arm calculated as  $\varphi_i = (\nu_i + \mu_i + \theta_i)$  and  $\nu_i = \frac{-\pi}{2}$  for  $i = 1, 2$  and  $\nu_i = \frac{\pm\pi}{2}$  for  $i = 3, 4$  and  $\mu_i = \{\frac{3\pi}{4}, \frac{\pi}{4}, \frac{-\pi}{4}, \frac{-3\pi}{4}\}$  for  $i = \{1, 2, 3, 4\}$  respectively. Along with (4) of main article, this gives the force estimate from spring action in  ${}_w\mathcal{F}$  frame.

### B. Boundedness and Convergence of the Wrench Estimator

In this section we comment on the stability of the wrench estimator which is actively employed by the primitive state machine. We prove that the wrench estimator is bounded at all times and converges to the arm-based estimate as  $t \rightarrow \infty$ . Let  $\hat{\delta}_{f_a} = \sum_{i=1}^4 \hat{\delta}_{f_i}$  denote the estimate from the spring-based arm wrench.

*Assumption 1:* Boundedness of estimated signals  $\hat{\delta}_{f_{CoM}}$  and  $\hat{\delta}_{f_a}$  and their derivatives  $\dot{\hat{\delta}}_{f_{CoM}}$ ,  $\dot{\hat{\delta}}_{f_a}$ . We assume that the individual estimates from the acceleration-based method employed on the UAV and the spring-damper arm are bounded.

*Remark 1:* Considering that most real-world estimators such as those proposed in [23] are employed for force feedback control, it is reasonable to assume that acceleration-based methods are bounded and provide bounded estimates even in the presence of uncertainties.

*Assumption 2:* The derivative of  $\dot{\hat{\delta}}_{f_{CoM}} \rightarrow 0$  as  $t \rightarrow \infty$ .

*Remark 2:* The acceleration-based dynamics are second-order dynamics and hence it is assumed that the signal  $\dot{\hat{\delta}}_{f_{CoM}}$  converges to a bounded value, hence the rate of change at the convergence is near zero.

*Proposition:* If  $\kappa_f$  is chosen such that:

$$\kappa_f = h(\dot{\hat{\delta}}_{f_{CoM}})$$

where  $h(\cdot)$  is a function that continuously increases from 0 to 1 as the magnitude of  $\dot{\hat{\delta}}_{f_{CoM}}$  decreases, then  $\kappa_f \rightarrow 1$  if  $\dot{\hat{\delta}}_{f_{CoM}} \rightarrow 0$  and vice-versa. This allows for the estimate to be bounded at all times.

*Proof:* We now discuss the boundedness and convergence (steady state) of the proposed wrench estimator via a break-up into following three different stages.

- 1) *Steady-state phase:* From *Assumption 2*, in the steady-state phase, the  $\dot{\hat{\delta}}_{f_{CoM}} \rightarrow 0$  and hence the proposed estimator will converge to the arm-based one, that is  $\hat{\delta}_f \rightarrow \hat{\delta}_{f_a}$ .
- 2) *Transient phase:* In the transient phase,  $\dot{\hat{\delta}}_{f_{CoM}} \rightarrow 1$  and hence the proposed estimator will converge to the CoM-based one, that is  $\hat{\delta}_f \rightarrow \hat{\delta}_{f_{CoM}}$ .
- 3) *Transition between transients and steady-state:* Finally by ensuring that  $h(\cdot) \in [0, 1]$  is a smooth function and

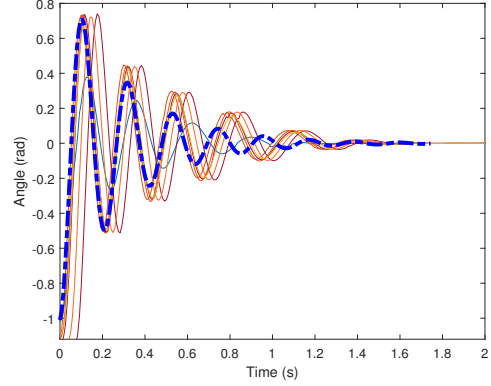


Fig. 9. Arm dynamics characterization with a step input. The system identification is done in MATLAB to obtain the damping and spring coefficients.

from *Assumptions 1 and 2*, the force estimate from the proposed estimator is bounded at all times.

### C. System Identification for Arm Dynamics

For the system identification of the arm dynamics, the inertia about  $z$ -axis for the arm,  $\mathcal{J}_{zz}$  was calculated using SolidWorks to be  $0.0015\text{kgm}^2$ . We design an experiment where the base of the XPLORER is held by a clamp and the torsional spring-based arm is first loaded to a certain fixed position using a force sensor. Then it is released and the motion capture system is used to generate the trajectory of the arm. We then use the MATLAB System ID toolbox to obtain the  $b$  and  $k$  values as 0.009 and 1.307 for  $\mathcal{J}_{zz} = 0.0015\text{kgm}^2$  in (4).

### D. Algorithms

This section presents the algorithms for *Exploration*, *Tactile turning* and *Tactile-traversal* in an algorithmic format. The position and yaw reference before current time-step is denoted by  $[x_{sp}^*(k) \ \psi^*(k)]^T$  and is used to reshape the reference at current step,  $[x_{sp}(k) \ \psi(k)]^T$ . Furthermore, we transform the reference into the inertial frame whenever necessary via

$$[x_{sp}^b \ y_{sp}^b \ z_{sp}^b]^T = {}_b^w\mathbf{R}[x_{sp} \ y_{sp} \ z_{sp}]^T \quad (10)$$

where  $[x_{sp}^b \ y_{sp}^b \ z_{sp}^b]^T$  denote the reference in the body frame,  ${}_b\mathcal{F}$ , and  $[x_{sp} \ y_{sp} \ z_{sp}]^T$  denote them in inertial frame  ${}_w\mathcal{F}$ . Similarly, 10 is also used to calculate the current position in body frame,  $x^b$ , from current position in inertial frame,  $x$ .

---

#### Algorithm 1: Exploration

---

**Input:**  $x^b, [x_{sp}^* \ \psi_{sp}^*]^T, \dot{\psi}$  &  $\hat{\delta}_f^b$   
**Output:**  $[x_{sp}^b \ \psi_{sp}]^T$  &  $\Gamma$   
**Parameters:**  $d_{step}$

- 1 **if**  $|\dot{\psi}| < \dot{\psi}_o$  &  $|\hat{\delta}_f^b| < \delta_0$  **then**
- 2      $x_{sp}^b(k) = x^b(k) + d_{step}$   
 $y_{sp}^b(k) = (y_{sp}^*)^b(k)$   
 $\psi_{sp}(k) = \psi_{sp}^*(k)$
- 3 **else if**  $|\dot{\psi}| > \dot{\psi}_o$  **then**
- 4      $\Gamma = 2$
- 5 **else**
- 6      $\Gamma = 3$

**Algorithm 2:** Tactile Turning

---

**Input:**  $[x_{sp}^* \psi_{sp}^*]^T, \dot{\psi}$  &  $\hat{\delta}_f^b$   
**Output:**  $[x_{sp} \psi_{sp}]^T$  &  $\Gamma$   
**Parameters:**  $\mathcal{W}, dt$

```

1 if  $|\dot{\psi}| > \psi_0$  &  $|\hat{\delta}_f^b| < \delta_{\psi_0}$  then
2    $x_{sp}(k) = x_{sp}^*(k)$ 
    $\dot{\psi}_{sp}(k) = sgn(\dot{\psi})\mathcal{W} \cdot dt$ 
3 else
4    $\Gamma = 3$ 

```

---

**Algorithm 3:** Tactile Traversal

---

**Input:**  $x^b, \dot{\psi}, [x_{sp}^* \psi_{sp}^*]^T$  &  $\hat{\delta}_f^b$  &  $\hat{\delta}_\tau^{e3}$   
**Output:**  $[x_{sp} \psi_{sp}]^T$  &  $\Gamma$   
**Parameters:**  $\delta_0, \delta_{f,des}$

```

1 Function CollisionNormal():
2   if  $\lambda = "+X" or "-X"$  then
3     if  $\hat{\delta}_f^{b1} > \delta_0$  then
4        $C_n = [1, 0, 0, 0]$ 
5     else if  $\hat{\delta}_f^{b1} < -\delta_0$  then
6        $C_n = [0, 1, 0, 0]$ 
7   else if  $\lambda = "+Y" or "-Y"$  then
8     if  $\hat{\delta}_f^{b2} > \delta_0$  then
9        $C_n = [0, 0, 1, 0]$ 
10    else if  $\hat{\delta}_f^{b2} < -\delta_0$  then
11       $C_n = [0, 0, 0, 1]$ 
12  return  $C_n$ 
13 Function MoveDirection():
14    $C_n \leftarrow$  ContactNormal()
15   if  $C_n == [1, 0, 0, 0]$  then
16      $\lambda = "+Y"$ 
17   else if  $C_n == [0, 1, 0, 0]$  then
18      $\lambda = "-Y"$ 
19   else if  $C_n == [0, 0, 1, 0]$  then
20      $\lambda = "-X"$ 
21   else if  $C_n == [0, 0, 0, 1]$  then
22      $\lambda = "+X"$ 
23   return  $\lambda$ 
24 Function TrajectoryGeneration():
25    $\lambda \leftarrow$  MoveDirection()
26    $\psi_{sp} = \psi_{sp}^*$ 
27   if  $\lambda = "+X"$  then
28      $x_{sp}^b(k) = x^b + d_{step}$ 
29      $\delta_{f,des} = [0 \Delta_{f,des} 0]^T, \delta_{\tau,des} = \hat{\delta}_\tau^{e3}$ 
30      $x_{sp}(k) = \text{AdmittanceController}(\delta_{f,des}, \delta_{\tau,des})$ 
31   else if  $\lambda = "-X"$  then
32      $x_{sp}^b(k) = x^b - d_{step}$ 
33      $\delta_{f,des} = [0 -\Delta_{f,des} 0]^T, \delta_{\tau,des} = \hat{\delta}_\tau^{e3}$ 
34      $x_{sp}(k) = \text{AdmittanceController}(\delta_{f,des}, \delta_{\tau,des})$ 
35   else if  $\lambda = "+Y"$  then
36      $y_{sp}^b(k) = y^b + d_{step}$ 
37      $\delta_{f,des} = [\Delta_{f,des} 0 0]^T, \delta_{\tau,des} = \hat{\delta}_\tau^{e3}$ 
38      $x_{sp}(k) = \text{AdmittanceController}(\delta_{f,des}, \delta_{\tau,des})$ 
39   else if  $\lambda = "-Y"$  then
40      $y_{sp}^b(k) = y^b - d_{step}$ 
41      $\delta_{f,des} = [-\Delta_{f,des} 0 0]^T, \delta_{\tau,des} = \hat{\delta}_\tau^{e3}$ 
42      $x_{sp}(k) = \text{AdmittanceController}(\delta_{f,des}, \delta_{\tau,des})$ 
43 Function Main():
44   CollisionNormal()
45   MoveDirection()
46   TrajectoryGeneration()

```

---

**Algorithm 4:** Mapping Framework

---

**Input:**  $[x, y, z]^T, \psi, \hat{\delta}_f^b, C_n$  &  $\lambda$   
**Output:** Point Cloud Data  
**Parameters:**  $\delta_{map}$

```

1 if  $|\hat{\delta}_f^b| \geq \delta_{map}$  then
2   if  $\lambda(k-1) \neq \lambda(k)$  then
3     Add Corner Block to Point Cloud
4   else
5     Add Obstacle to Point Cloud in  $C_n$  axis
6 else
7   Store Point Cloud Data

```

---

*Note:* In all the algorithms presented above,  $\text{AdmittanceController}()$  refers to the implementation of (8) of the main article, the interaction controller that reshapes the position and yaw reference based on the desired interaction wrench.

*E. Time-optimal control with state jumps*

1) *Problem setup:* Consider the following double integrator dynamics for a continuous-time system with states  $\tilde{x} \in \mathbb{R}^2$ :

$$\begin{aligned} \dot{\tilde{x}}_1 &= \tilde{x}_2 \\ \dot{\tilde{x}}_2 &= u \end{aligned} \quad (11)$$

It is assumed that the jump pattern is induced by the flow set  $\mathcal{C} := \{\tilde{x} \in \mathbb{R}^2\}$  and the jump set which denotes the states where XPLORER undergoes collision and hence has a discontinuity in its state as defined by:

$$\mathcal{D} = \{\tilde{x} \in \mathbb{R}^2 | \tilde{x}_1 = a, \tilde{x}_2 \leq 0\}, \quad (12)$$

where  $a$  is the location of object that XPLORER can collide on. Furthermore, let the hybrid system be described by:

$$\begin{aligned} \dot{\tilde{x}} &= \mathbf{A}\tilde{x} + \mathbf{B}u & \tilde{x} \in \mathcal{C} \\ \tilde{x}^+ &= \mathbf{E}\tilde{x} & \tilde{x} \in \mathcal{D} \end{aligned} \quad (13)$$

where  $\mathbf{A} \in \mathbb{R}^{2 \times 2}$  is the state matrix,  $\mathbf{B} \in \mathbb{R}^{2 \times 1}$  is the input matrix and  $\mathbf{E} \in \mathbb{R}^{2 \times 2}$  denotes the state evolution during the jump.

The conventional time-optimal control for a system to reach  $(0, 0)$  from a state  $\tilde{x}_0$  is given by the *bang-bang* control law where the control only takes the values  $\{-1, 1\}$  and at most one switch is required. More specifically, the trajectories are characterized by the family of the parabolas:

$$\begin{cases} u = +1 & \begin{cases} \tilde{x}_1(t) = +\frac{1}{2}t^2 + \alpha t + \beta \\ \tilde{x}_2(t) = +t + \alpha \end{cases} \\ \tilde{x}_1 = \frac{1}{2}\tilde{x}_2^2 + \beta - \frac{\alpha^2}{2} & \begin{cases} u = -1 \\ \tilde{x}_1(t) = -\frac{1}{2}t^2 + \alpha t + \beta \\ \tilde{x}_2(t) = -t + \alpha \end{cases} \\ \tilde{x}_1 = -\frac{1}{2}\tilde{x}_2^2 + \beta - \frac{\alpha^2}{2} & \end{cases}$$

with the switching curve  $\Pi := \{\tilde{x} : \tilde{x}_1 + \frac{1}{2}\tilde{x}_2|\tilde{x}_2|\}\}$  and parameters  $\alpha, \beta$ . Furthermore, given the initial condition, the optimal time is given by:

$$t_0^*(\tilde{x}_0) = \begin{cases} 2\sqrt{\frac{1}{2}\tilde{x}_{20}^2 + \tilde{x}_{10}} + \tilde{x}_{20}, \tilde{x}_0 \in S^- \\ |\tilde{x}_{20}|, \tilde{x}_0 \in \Pi \\ 2\sqrt{\frac{1}{2}\tilde{x}_{20}^2 - \tilde{x}_{10}} - \tilde{x}_{20}, \tilde{x}_0 \in S^+ \end{cases} \quad (14)$$

where  $\mathbb{R}^2 = S^- \cup \Pi \cap S^+$ ,  $S^\pm$  stands for the regions below and above the switching curve  $\Pi$ .

2) *Time optimal control with 1 state jump due to collisions*: We now extend the analysis to study the case scenarios where collisions induce a state jump in velocity. For this case the, let the jump map  $\mathbf{E}$  be given by:

$$\mathbf{E} = \begin{bmatrix} 1 & 0 \\ 0 & e \end{bmatrix} \quad (15)$$

where  $e$  stands for the coefficient of post collision velocity as a function of the coefficient of restitution. The data-driven model in the Section -F is used to predict the post-collision state. This value  $e$  can be obtained using a linearization of the collision model. Then any generic point  $\tilde{z}$  on the jump set  $\mathcal{D}$  can be denoted by  $\tilde{z} = (a, \zeta)$  where  $a$  denotes the position of the wall and  $\zeta$  denotes the pre-collision velocity. The optimal path to  $\tilde{z}$  from any given initial point  $\tilde{x}_0$  are given by the two branches of parabolas with a switching curve passing through  $\tilde{z}$  as [44];

$$\Phi(\zeta) = \{\tilde{x} : \frac{1}{2}(\tilde{x}_2 + \zeta)|\tilde{x}_2 - \zeta| - a + \tilde{x}_1\}$$

We can again decompose the state space as:

$$\mathbb{R}^2 = \Psi^- \cup \Phi \cap \Psi^+,$$

where  $\Psi^\pm$  is similarly defined as the regions below and above the switching curve  $\Phi$ . The optimal time taken to reach  $\tilde{z}$  from  $\tilde{x}_0$  can then be written as:

$$\tau(\tilde{x}_0, \zeta) = \begin{cases} \left| \zeta + \sqrt{\frac{\zeta^2}{2} + \frac{\tilde{x}_{20}^2}{2} - a + \tilde{x}_{10}} \right| + \tilde{x}_{20} & \tilde{x}_0 \in \Psi^+(\zeta), \\ + \sqrt{\frac{\zeta^2}{2} + \frac{\tilde{x}_{20}^2}{2} - a + \tilde{x}_{10}}, & \tilde{x}_0 \in \Phi(\zeta), \\ \left| \tilde{x}_{20} - \zeta \right|, & \tilde{x}_0 \in \Phi(\zeta), \\ \left| \zeta - \sqrt{\frac{\zeta^2}{2} + \frac{\tilde{x}_{20}^2}{2} + a - \tilde{x}_{10}} \right| - \tilde{x}_{20} & \tilde{x}_0 \in \Psi^-(\zeta), \\ + \sqrt{\frac{\zeta^2}{2} + \frac{\tilde{x}_{20}^2}{2} + a - \tilde{x}_{10}}, & \tilde{x}_0 \in \Psi^-(\zeta) \end{cases} \quad (16)$$

The corresponding optimal control law is given as:

$$u_1^* = \begin{cases} 1, & \text{if } j = 0, \gamma_0(\tilde{x}(t, 0)) < 0 \\ -1, & \text{if } j = 0, \gamma_0(\tilde{x}(t, 0)) > 0 \\ -sgn(\tilde{x}_2(t, 0) - z_2^*(\tilde{x}_0)), & \text{if } j = 0, \gamma_0(\tilde{x}(t, 0)) = 0 \\ 1, & \text{if } j = 1, \gamma_1(\tilde{x}(t, 1)) < 0 \\ -1, & \text{if } j = 1, \gamma_1(\tilde{x}(t, 1)) > 0 \\ -sgn(\tilde{x}_2(t, 1)), & \text{if } j = 1, \gamma_1(\tilde{x}(t, 1)) = 0 \end{cases} \quad (17)$$

where the functions  $\gamma_0 : \mathbb{R}^2 \rightarrow \mathbb{R}$  and  $\gamma_1 : \mathbb{R}^2 \rightarrow \mathbb{R}$  are defined as follows:

$$\begin{aligned} \gamma_0(\tilde{x}) &= \frac{1}{2}(\tilde{x}_2 + z_2^*(\tilde{x}_0))|\tilde{x}_2 - z_2^*(\tilde{x}_0)| - z_1^*(\tilde{x}_0) + \tilde{x}_1 \\ \gamma_1(\tilde{x}) &= \tilde{x}_1 + \frac{1}{2}\tilde{x}_2|\tilde{x}_2| \end{aligned}$$

Furthermore, the 1-jump minimum time is given by [44]

$$t_1^*(\tilde{x}_0) = \min_u \{\tau(\tilde{x}_0, \zeta) + t_0^*(\mathbf{E}\tilde{z})\} \quad (18)$$

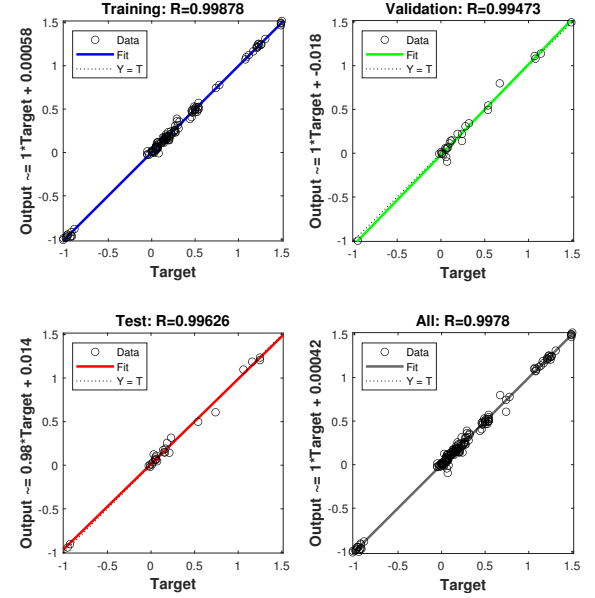


Fig. 10. Validation results for the collision neural network showing the  $R^2$  values obtained for the trained model. We see that the trained network is able to predict the post collision state with high accuracy.

where  $\mathbf{E}\tilde{z}$  denotes the post collision state. The proof follows the approach used in [44]. We now use this result to calculate the 1-jump minimum time and select between collision-free and collision-inclusive trajectories.

*Remark 3:* For our experiments, we only select ricocheting if the collision-based travel time—calculated as the time to reach the collision node at maximum velocity plus the time from the post-collision velocity to the goal—is shorter than a direct flight under P-PID control. We begin by choosing the maximum velocity XPLORER can attain (from a discrete set) in the closed flight space and verify via the CollisionNet that a reduced rebound state is indeed generated post-collision. Intuitively,  $\zeta$  is both upper- and lower-bounded: it must not be so large that traveling to the collision node inflates total maneuvering time, nor so small that it prematurely diverts the UAV from its course. We will derive these bounds formally in our future work.

3) *Illustrative example for time-optimal state jumps*: In this subsection we present an example to illustrate the minimum time trajectories obtained with collisions. For this particular example, we assume the coefficient of restitution  $e = -0.6$  in (15). Consider a wall at  $a = 0.5$ , and an initial state  $\tilde{x}_0 = [-1 2]^T$  as shown by the diamond marker in Fig. 5 right. For the double integrator system, the right-open parabolic curves show the trajectories when maximum available control,  $\tilde{u} = 1$  is applied. Similarly, the left-open parabolic curves denote the system trajectory when minimum control  $\tilde{u} = -1$  is applied. Consequently, the the 0-jump minimum time which corresponds to *bang-bang* control law can be calculated using (14) as 4 seconds and shown by the path 1-4-5 red-magenta curved trajectory in Fig. 5 right where the maximum deceleration-based trajectory was followed until it intersects the switching curve, here shown by the magenta curve and acceleration was applied to reach to (0,0).

Now to understand the trajectory generated by the collision-inclusive planner, consider any generic point  $(a, \zeta)$  after collision translates to  $(a, -e\zeta)$ , therefore the minimum time to reach  $(0, 0)$  from an initial location  $\tilde{x}_0 = [-1 2]^T$ , by undergoing collision and then employing maximum deceleration can be calculated using (16) as 1.756 seconds with  $\zeta^* = 1.667$  for  $e = 0.6$ . The corresponding *bang-bang-jump-bang* trajectory is shown in Fig. 5 right. If there was no collision, XPLORE would have taken the trajectory shown by the path 1-4-5 to reach  $(0,0)$  in minimum time. However with a state-jump available, the optimal solution is to include the state-jump and undergo collision. Hence, XPLORE first reaches the wall with an optimal  $\zeta^*$  velocity as calculated by argmin of (18) by using *bang-bang* control as shown by the blue lines. It then undergoes the state transition governed by  $E$  to reach the point shown by the black star after which it again follows the black switching curve to reach to the origin  $(0,0)$ . This path is shown by the path 1-2-3-4-5, blue-magenta curved lines, in Fig. 5 right. The trajectory 1-2 is obtained by accelerating, 2-3 is obtained by decelerating and hitting the wall with the optimal velocity and post collision state is 3-4 and finally acceleration is applied to reach to  $(0,0)$ .

#### F. CollisionNet- A Neural Network for post-collision state

From the set of 60 experiments, a data-driven collision model was developed to study the effects of collisions at various intensities and various angle of incidence for XPLORE. The experimental data collected are plotted as the pre-collision and post-collision velocities in Fig. 5 left of main article. This collision model is crucial to identify the coefficient of restitution and the post-collision state of the vehicle for trajectory planning. Since the collisions for the deformable vehicle are highly nonlinear, a nonlinear regression model using neural networks was employed to develop the collision model- CollisionNet. MATLAB Deep Learning Toolbox (MATLAB R2021b) was employed for the training using Levenberg-Marquardt method. Five features were identified to train the model: the  $v_x^-, v_y^-$  representing pre-collision state, angle of incidence to the collision plane, and type of collision. The angle of incidence is a function of the orientation of the vehicle, while the type of collision is either collide-to-stop (inelastic collision) or collide-to-decelerate (elastic collision). We choose 75% of the dataset for training and 25% for validation. The results for the CollisionNet are given in Fig. 10 and we see that the accuracy is very high with a  $R^2$  value of 0.99.

It is noticed from Fig. 5 that for different angles and same pre-collision state, the post collision state is always very similar. This shows that for this particular quadrotor design, angle of collision is not a critical parameter to model and hence justifies our assumption to use a point-mass based double integrator model to ricochet.

#### G. Additional results for rigid quadrotor

In this section we present results for exploration experiments with a rigid quadrotor of the same dimensions. The same exploration scheme developed for XPLORE was offloaded

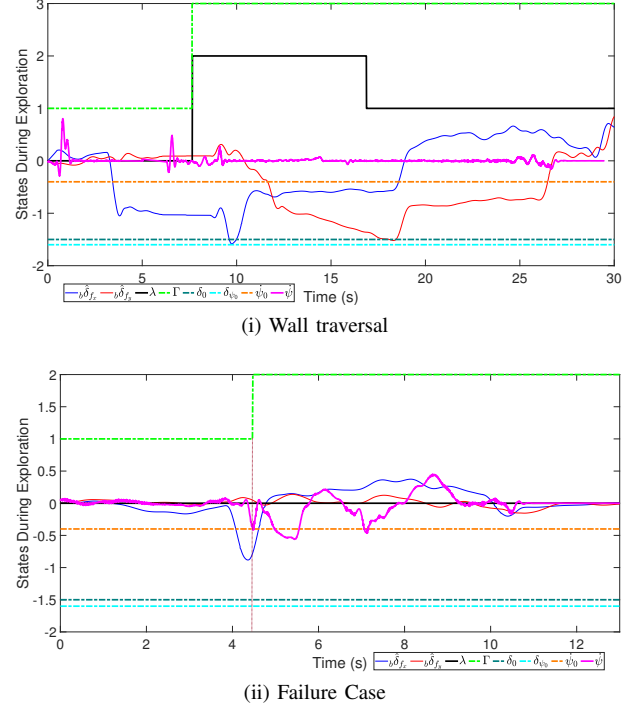


Fig. 11. Exploration results for two case scenarios for rigid UAV. (a) shows the results for exploration of a wall-like structure. The rigid UAV performs as desired, and the exploration states  $\Gamma = 1, 3$  are duly activated. (b) shows the results for cases when the force and torque at initial contact is so high, such that the yaw torque leads to engaging the *Tactile-turning* state with  $\Gamma = 2$  and fails to start the exploration with  $\Gamma = 3$  that is *Tactile-traversal*.

to a rigid quadrotor to check the performance for exploration. We conducted both wall-traversal and the box-traversal experiments out of which only the wall-traversal succeeded with the rigid quadrotor.

For the wall traversal results shown in Fig. 11i, the rigid UAV takes off and upon making initial contact, applies the desired force on the wall and initiates the *Tactile-traversal*. When it detects the second wall, it engages the traversal motion in the body  $+Y$  direction as shown by the black line.

Finally, another unpredictable behavior was observed with the rigid UAV, as shown in Fig. 11ii. Sometimes when the rigid UAV makes impact, due to the high rebound velocities, and the presence of yaw admittance control given by (8), there is a high yaw-rate which falsely triggers the *Tactile-turning* and the entire exploration fails. However this behavior is not observed with the XPLORE due to the damping effect and shock-absorbing nature of the torsion spring in the arm.